ACS APPLIED MATERIALS & INTERFACES

www.acsami.org

Research Article

Novel Charging-Optimized Cathode for a Fast and High-Capacity Zinc-Ion Battery

Zhi Li,[▽] Buke Wu,[▽] Mengyu Yan, Liang He, Lin Xu, Guobin Zhang, Tengfei Xiong, Wen Luo,* and Liqiang Mai

Cite This: *ACS Appl. Mater. Interfaces* 2020, 12, 10420−10427

Read Online

ACCESS | Metrics & More | Article Recommendations | Supporting Information

ABSTRACT: A rechargeable aqueous zinc-ion battery (ZIB) is one of the attractive candidates for large-scale energy storage. Its further application relies on the exploitation of a high-capacity cathode and the understanding of an intrinsic energy storage mechanism. Herein, we report a novel layered $K_2V_3O_8$ cathode material for the ZIB, adopting a strategy of charging first to extract part of K-ions from vanadate in initial few cycles, which creates more electrochemically active sites and lowers charge-transfer resistance of the ZIB system. As a result, a considerable specific capacity of 302.8 mA h g^{-1} at 0.1 A g^{-1}, as well as a remarkable cycling stability (92.3% capacity retention at 4 A g^{-1} for 2000 cycles) and good rate capability, are achieved. Besides, the energy storage mechanism was studied by in situ X-ray diffraction, in situ Raman spectroscopy, X-ray photoelectron spectroscopy, and inductively coupled plasma mass spectroscopy. An irreversible K-ion deintercalation in the first charge process is proved. It is believed that this novel cathode material for the rechargeable aqueous ZIB and the optimizing strategy will shed light on developing next-generation large-scale energy storage devices.

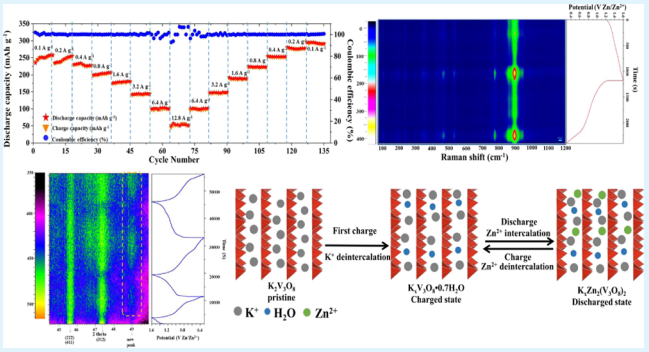

KEYWORDS: *zinc-ion battery, $K_2V_3O_8$, in situ X-ray diffraction, in situ Raman spectra, high performance cathode*

1. INTRODUCTION

Because of the ever-worsening environmental pollution and depletion of fossil fuels, the requirements for renewable energy are increasingly in demand.[1−3] Among the large-scale energy storage systems, lithium-ion batteries involving organic electrolytes are the most extensively applied devices in infrastructures.[4−9] However, the issues of processing costs, safety problems, and limited lithium resources still remain to be solved.[10−12]

Among many types of energy storage systems, rechargeable aqueous zinc-ion batteries (ZIBs) have attracted much attention for their safety, low cost, environmental friendliness, and a remarkable theoretical capacity (819 mA h g^{-1} based on Zn anode).[13−27] Many cathode materials, such as MnO_2,[18] vanadate,[15,17,19] and Prussian blue analogues,[24−26] have been intensively explored. The unsatisfactory rate performance and poor cycling stability, however, limit their further practical applications, usually caused by the degradation of cathode materials.[27−29] Therefore, it is of great significance to explore novel cathode materials and advanced technology for ZIBs.

Until now, there are two dominant strategies to improve the electrochemical performance of ZIBs. First, by preintercalating metal cations or organic molecules, the interplanar crystal spacing of the cathode material is changed (increases in most cases).[30−34] Meanwhile, the noncovalent bonds are formed between preintercalation cations and interlayer oxygen atoms to reduce the deformation of crystal structure. For example, Wang et al. found that by inserting polyaniline in the interplanar spacing of the MnO_2 nanosheet, the crystal structure of the cathode material becomes more stable, and the irreversible phase transformation is inhibited with the increased electrical conductivity.[35] Second, by combining cathode materials with carbonaceous materials (graphene, carbon fiber, etc.) to increase the conductivety of the cathode.[36−38] Mai et al. successfully synthesized MnO_2@graphene oxide nanowires; furthermore, the electrical conductivity and the electrochemical performance of the MnO_2 nanowires are improved greatly after coating with graphene scroll.[37]

Different from the optimizing methods mentioned above, herein a novel $K_2V_3O_8$ as the cathode material for ZIBs is reported. Unlike other preintercalation cathode materials, $K_2V_3O_8$ has two K-ions per formula unit between the layers of vanadium oxide. Inspired by this potassium-rich structure,

Received: November 27, 2019
Accepted: February 7, 2020
Published: February 7, 2020

https://dx.doi.org/10.1021/acsami.9b21579
ACS Appl. Mater. Interfaces 2020, 12, 10420−10427

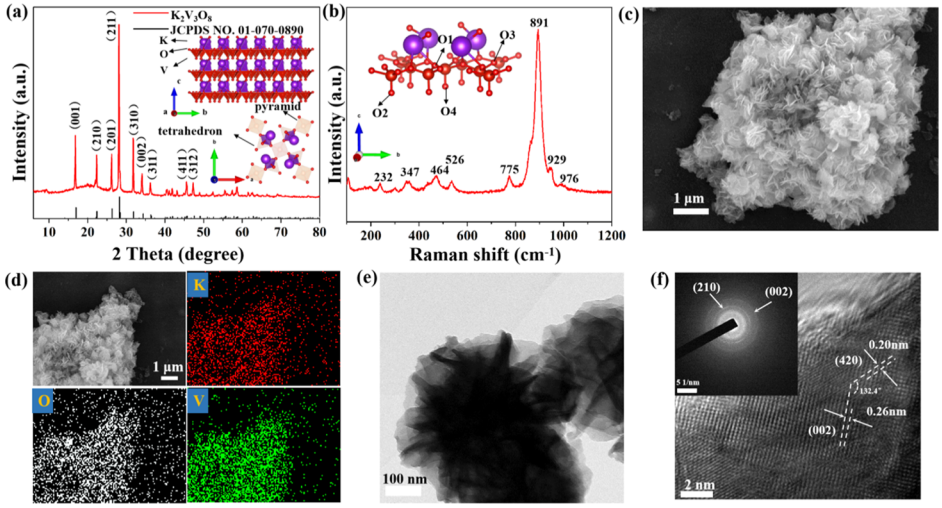

Figure 1. (a) XRD pattern and the crystal structure sketch of $K_2V_3O_8$. (b) Raman spectrum and molecular structure sketch of $K_2V_3O_8$. (c) SEM image of the $K_2V_3O_8$ nanoflower. (d) SEM/EDS element mapping. (e) TEM image, (f) HRTEM and (inset) SAED image of as-synthesized $K_2V_3O_8$.

we first charge the assembled battery to 1.6 V rather than discharge. In the initial few charge−discharge processes, the K-ions are extracted from the interlayer of the layered $K_2V_3O_8$ material, similar to the inversed way of the preintercalation procedure. In situ X-ray diffraction (XRD), in situ Raman spectroscopy, X-ray photoelectron spectroscopy (XPS), thermogravimetric analysis (TGA), and inductively coupled plasma mass spectroscopy (ICP-MS) were applied to study the energy storage mechanism. It is demonstrated that the cathode material undergoes crystal structure amorphization and irreversible K-ion extraction during the initial cycles. After these activating processes, the electrical conductivity of the cathode is improved dramatically. As a result, the assembled Zn//$K_2V_3O_8$ battery achieves a remarkable specific capacity of 302.8 mA h g^{-1} (at 0.1 A g^{-1} current density), a considerable cycling stability (92.3% retention under 4 A g^{-1} for 2000 cycles), as well as extraordinary rate capability, which is much higher than that of most of the other potassium vanadates previously published.[33]

2. MATERIALS AND METHODS

2.1. Material Preparation. All raw materials applied in the synthesis process are of analytical grade (AR) and purchased form Aladdin Bio-Chem Technology Company (Aladdin, Shanghai, China). First, 2.4 mmol KOH and 1.8 mmol V_2O_5 were mixed and dissolved in 70 mL of deionized (DI) water under constant stirring for 20 min. Then, the reactants were moved into a 100 mL Teflon-lined autoclave and kept at 200 °C for 48 h. As the hydrothermal reaction completed, the mixture was cooled down to ambient temperature. Then, the obtained precipitation was extracted by centrifugation, followed by washing with ethyl alcohol five times, and dried in a 80 °C vacuum oven for 48 h. The average yield of the final products for each batch is 0.25 g.

2.2. Material Characterization. The crystal structure of the as-prepared $K_2V_3O_8$ was tested through a Bruker D8 Discover X-ray diffractometer with Cu Kα radiation (λ = 1.5406 Å); the step time for collecting each data was 480 s. Raman measurement was done by HORIBA HR Evolution; the wavelength of the laser is 633 nm. The morphologies and submicroscopic images were collected by a field emission scanning electron microscope (FESEM, JSM-7100F) and a transmission electron microscope (TEM, JEOL JEM-2100F STEM/EDS microscope). Energy-dispersive X-ray spectroscopy (EDS) characterization was operated by Oxford EDS IE250. XPS testing was performed on Thermo Scientific ESCALAB 250Xi; the cathode plates were washed by DI water three times and dried before characterization. TGA (STA-449C) was conducted for measuring the quality change of the cathode material at different electrochemical states in Ar atmosphere with a temperature ramp of 5 °C min^{-1}; the electrodes were dried at 85 °C for 48 h before testing. ICP-MS was used to confirm the mass (%) and substance amount change of K and V elements of the cathode material during the charge−discharge process of first cycle, and the involved equipment was JY/T015-1996.

In situ XRD was performed by a Bruker D8 Discover X-ray diffractometer mentioned before, with a step time of 180 s for collecting each data, and the characterization window on the cathode surface of the mold battery was sealed by a plastic wrap.

In situ Raman measurement was performed by HORIBA HR Evolution; the wavelength of the laser is 633 nm. A mold battery was used during the testing; we used sapphire glass as the window to allow the laser reach the cathode, and the current collector is a Ti foil with a hole in the middle for the laser. The signals were received by a planar detector (still mode) during the electrochemical process. The step time for each pattern is 80 s.

2.3. Electrochemical Characterization. The $K_2V_3O_8$ cathode was synthesized through adding the mixture of prepared $K_2V_3O_8$ (37.5 mg, 75 wt %), acetylene black (10 mg, Super P, 20 wt %), and polyvinylidene fluoride (2.5 mg, 5 wt %) together with 0.4 mL of *N*-methyl-2-pyrrolidone as the solvent, and then, the mixture was transferred to an ultrasonic machine for 4 h. The obtained slurry was uniformly pasted on a clean Ti foil and then cut into Φ10 mm disks. The mass loading of each cathode piece on the Ti foil is 0.9 mg (1.15 mg cm^{-2}). Zn foil, cleaned with ethanol, and abrasive paper served as the anode, and glass fiber was applied as a separator of the battery. Zinc trifluoromethylsulfonate [3 mol L^{-1}, $Zn(CF_3SO_3)_2$, Aladdin, AR, 99.9%] solution was applied as the electrolyte. The electrochemical characterizations were accomplished through assembling 2016-coin cells in air with the LAND battery characterization system (CT2002A). Cyclic voltammetry (CV) and electrochemical impedance spectroscopy (EIS) were performed on a CHI760E electrochemical workstation. The above characterizations were tested at room temperature.

3. RESULTS AND DISCUSSION

The $K_2V_3O_8$ sample was prepared by a hydrothermal reaction, and its morphology can be regulated by changing the concentrations of KOH and V_2O_5 (with a fixed molar proportion, KOH/V_2O_5 = 4:3). As shown in Figure S1, in general, the low reactant concentrations lead to a nanosheet

https://dx.doi.org/10.1021/acsami.9b21579
ACS Appl. Mater. Interfaces 2020, 12, 10420−10427

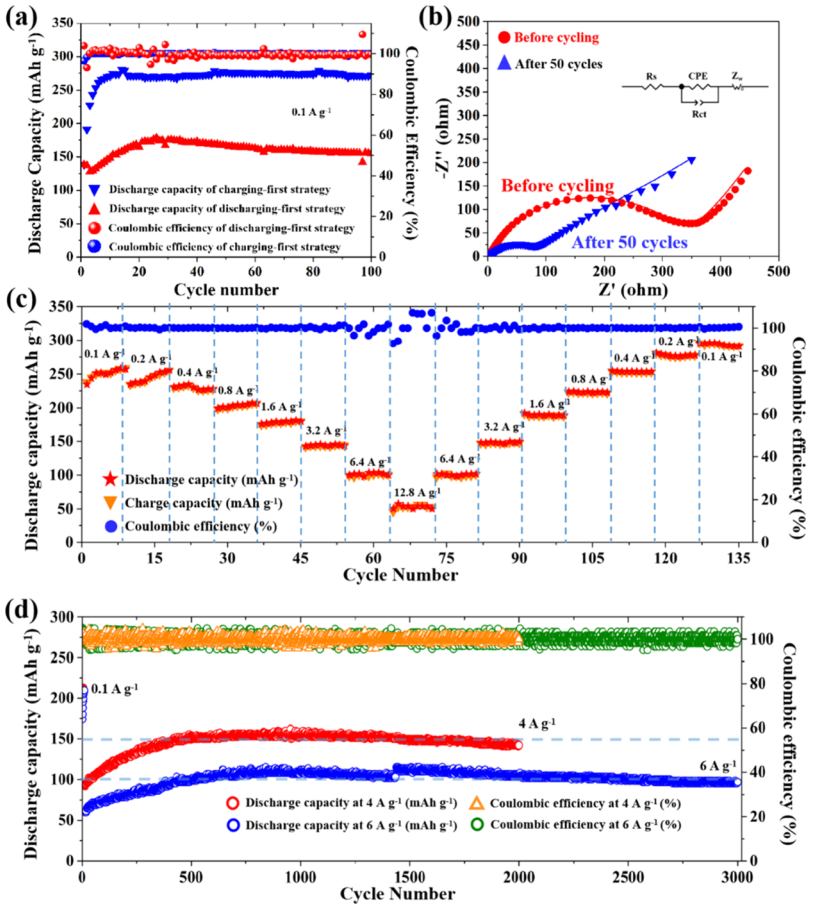

Figure 2. (a) Cycling performance of $K_2V_3O_8$ cathode adopting different strategies (at a current density of 0.1 A g^{-1}). (b) Nyquist plot and its fitted results of Zn//$K_2V_3O_8$ battery before cycling and at fully activated state. (c) Rate performance of $K_2V_3O_8$ at current densities between 0.1 and 12.8 A g^{-1}. (d) Cycling performance of $K_2V_3O_8$ at current densities of 4 and 6 A g^{-1} (1 C = 0.372 A g^{-1}).

morphology, while the morphology of the nanoflowers composed by nanosheets gradually forms as the reactant concentration increases. The sample synthesized by 1.8 mmol V_2O_5 and 2.4 mmol KOH was chosen for further characterization on account of the homogeneity of the morphology. Figure 1a exhibits the XRD pattern and crystal structure of $K_2V_3O_8$. All the diffraction peaks match well with the standard card JCPDS no. 01-070-0890, and the crystal structure schematically (inset of Figure 1a) indicates that the K-ions are located between the vanadium oxide layers, which consist of [VO_4] tetrahedra and a [VO_5] pyramid.

The Raman spectrum and the molecular structure of $K_2V_3O_8$ are shown in Figure 1b. The high-frequency modes (>500 cm^{-1}) are the V−O stretching vibration modes of the [VO_5] pyramid and the [VO_4] tetrahedra. $K_2V_3O_8$ has four different O sites and two different V sites (see the inset of Figure 1b): O1 (bridge of [VO_4] tetrahedra and [VO_5] pyramid), O2 (apical to [VO_4] tetrahedra), O3 (bridge of [VO_4] tetrahedra), and O4 (apical to [VO_5] pyramid). The highest frequency mode characterized at 976 cm^{-1} corresponds to the V−O4 stretching vibration mode of the [VO_5] pyramid. The 929 cm^{-1} band represents the V−O2 stretching vibration mode of the [VO_4] tetrahedra. The 891 and 526 cm^{-1} modes result from the stretching modes of vanadate and basic plane oxygen. The phonon modes within the range of 250 and 500 cm^{-1} are V−O−V and O−V−O bending vibrations. The lower frequency (<200 cm^{-1}) matches the twisting motions of the square pyramids and tetrahedra, along with K atom vibrations.[39−42]

The SEM and TEM images (Figure 1c,e) exhibit the homogeneous morphology of the $K_2V_3O_8$ nanoflower, stacked by nanosheets, with a diameter of 400−800 nm. The SEM/EDS characterization (Figure 1d) represents the uniform distribution of K, V, and O elements. Figure 1f shows the results of the selected area electron diffraction (SAED) and high-resolution TEM (HRTEM) of the $K_2V_3O_8$ nanoflower, the lattice spacing of 0.26 nm corresponds to the (002) crystal planes of $K_2V_3O_8$. In addition, the SAED (inset of Figure 1f) pattern confirms the polycrystalline structure of the prepared $K_2V_3O_8$.

For the purpose of investigating the electrochemical performance of the $K_2V_3O_8$ cathode, the Zn//$K_2V_3O_8$ battery was assembled using CR2016 coin-type cells. $Zn(CF_3SO_3)_2$ (3 mol L^{-1}) was chosen as the electrolyte salt. Instead of preintercalating K-ions into the vanadium framework interlayer, the potassium-rich cathode ($K_2V_3O_8$) is chosen to in situ deintercalate part of K-ions at the interlayer in the first charge process. It is expected that the electrochemical activation process can extract part of K-ions to provide more electrochemically active sites.

The performance achieved by adopting charging-first or discharging-first strategies is compared and displayed in Figure 2a. Under a low current density of 0.1 A g^{-1}, the Zn//$K_2V_3O_8$ battery by adopting the charging-first strategy displays a specific capacity of 281.3 mA h g^{-1}, but the specific capacity by

https://dx.doi.org/10.1021/acsami.9b21579
ACS Appl. Mater. Interfaces 2020, 12, 10420−10427

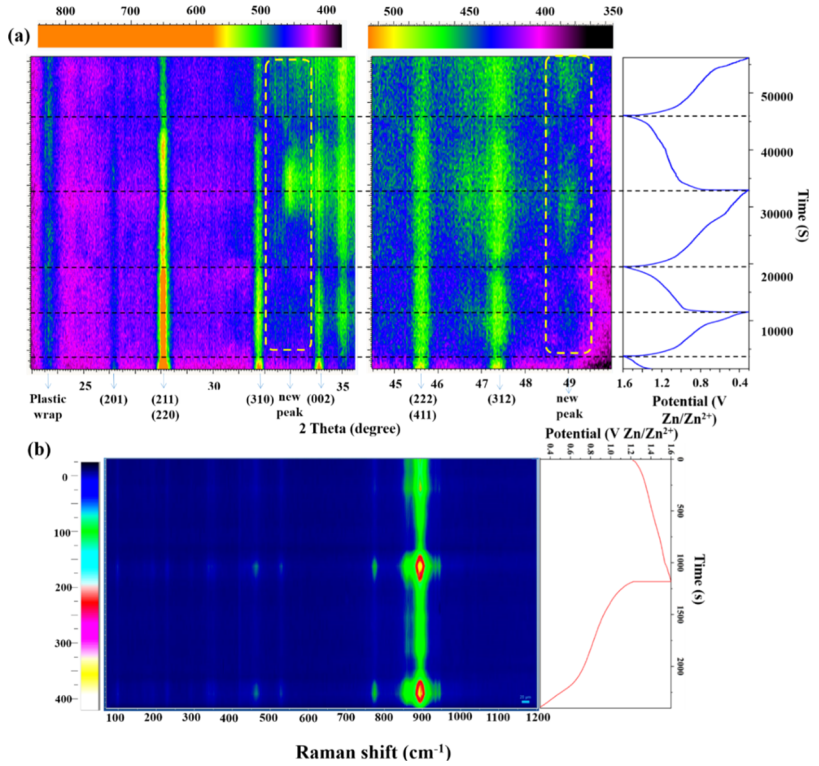

Figure 3. (a) Electrochemical in situ XRD characterization of the cathode of Zn//$K_2V_3O_8$ battery. (b) Electrochemical in situ Raman characterization of the cathode of Zn//$K_2V_3O_8$ ZIB for the initial cycle.

adopting the discharging-first strategy is only 176.1 mA h g^{-1}. It is obvious that the specific capacity observed by the charging-first strategy is much higher than that delivered by the discharging-first strategy.

Besides, through the charging-first strategy, the Zn//$K_2V_3O_8$ system experienced a shorter activation process (less than 15 cycles), whereby the capacity gradually increases and arrives at its stable state. Therefore, the electrochemical performance by adopting the charging-first strategy was studied in detail afterward. Figure S2a shows the charge−discharge curve of the aqueous Zn//$K_2V_3O_8$ battery during the initial charge−discharge process (at 0.1 A g^{-1}). Notably, the initial charging capacity is only 31.2 mA h g^{-1}, while the first discharge process exhibits a specific capacity of 138.5 mA h g^{-1}. This huge difference of specific capacity indicates an irreversible reaction occurring in the first charge−discharge process.

Figure 2b represents the EIS testing results of the initial state and full activation state of the Zn//$K_2V_3O_8$ battery. After full activation (under a current density of 0.1 A g^{-1}, 50 cycles), the fitting data indicate that the charge-transfer resistance (R_{ct}) of fully activated state (109 Ω) is much lower than that of the original state (402 Ω). The results indicate that the electrical conductivity is greatly improved after full electrochemical activation. This is also supported by the excellent rate performance (Figure 2c), and the Zn//$K_2V_3O_8$ battery exhibits the capacities of 302.8, 278.5, 250.1, and 225.3 mA h g^{-1} at 0.1, 0.2, 0.4, and 0.8 A g^{-1}, respectively. Under higher current densities of 3.2, 6.4, and 12.8 A g^{-1}, the high capacities of 148.6, 100.0, and 53.2 mA h g^{-1} are delivered. When comes to a considerably high current density of 12.8 A g^{-1}, the time for a single cycle of charge-discharge costs only 25 s. Figure S3 displays the charge−discharge curves of the Zn//$K_2V_3O_8$ battery under different current densities. As the rate increases, the charge plateaus move to the lower potential because of the higher polarization of the electrode. Compared with other representative cathode materials ($V_5O_{12}·6H_2O$,[22] $Zn_{0.25}V_2O_5$,[17] $K_2V_8O_{21}$,[33] α-MnO_2,[37] and VS_2[21]) for ZIBs (Figure S4), the $K_2V_3O_8$ nanoflower exhibits a remarkable high capacity under high current densities.[23] Figure 2d shows the long-term cycling stability. The Zn//$K_2V_3O_8$ battery achieves a capacity of 154.3 A g^{-1} with 92.4% capacity retention for 2000 cycles (at 4 A g^{-1}) and a capacity of 115.3 mA h g^{-1} with 86.9% capacity retention for 3000 cycles (at 6 A g^{-1}). It should be noted that the specific capacity of the battery shows an increasing tendency during cycling stability testing because of the sluggish penetration of the electrolyte and the gradual extraction of the K^+ ion during several cycles.[17,33]

The CV results of the Zn//$K_2V_3O_8$ battery shown in Figure S2b at scan rates from 0.1 to 0.4 mV s^{-1} suggest a multistep energy storage mechanism of Zn ions, with two pairs of redox peaks located at 1.10/0.83 and 0.64/0.48 V, respectively. As described in Figure S2b,c, a relevant analysis is performed to study the relationship of scan rate and peak current (i), based on eq 1.

$$i = av^b \tag{1}$$

The value of b = 0.5 implies that the semi-infinite linear diffusion is dominated by charge storage, and b = 1 implies a capacitive-controlled charge storage mechanism.[43−45] The b-value can be computed by calculating log(i) versus log(v) (Figure S2c). After linear fitting, the b-values of peaks 1, 2, 3, and 4 are 0.61, 0.58, 0.63, and 0.76, respectively, which are much closer to 0.5, indicating a diffusion-dominated process.

Unlike investigating other cathode materials for ZIBs, the strategy of charging first instead of discharging was adopted during the whole characterizations to create more electro-

https://dx.doi.org/10.1021/acsami.9b21579
ACS Appl. Mater. Interfaces 2020, 12, 10420−10427

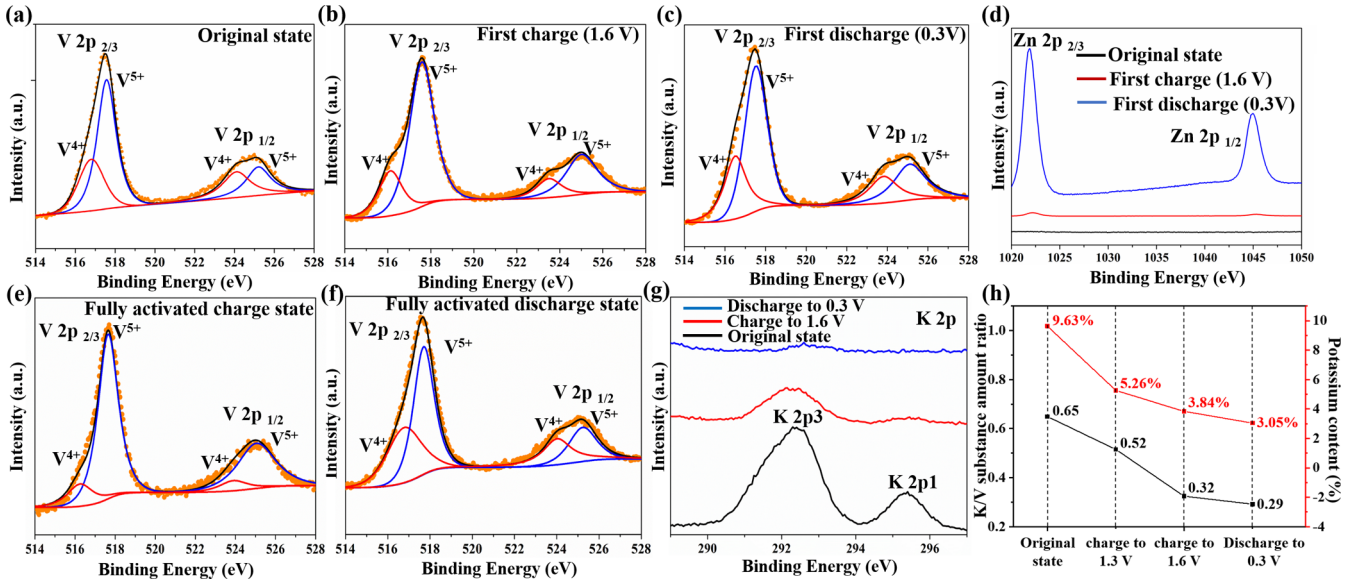

Figure 4. (a–d) XPS spectra of V and Zn elements of $K_2V_3O_8$ for the first cycle. (e) XPS spectra of V element of $K_2V_3O_8$ cathode at fully activated charged state and (f) fully activated discharged state. (g) XPS spectra of K element at different charge–discharge states of first cycle. (h) ICP characterization of K/V substance amount ratio and potassium content.

chemically active sites through extracting K-ions from the interlayers of vanadium oxide. To better understand the energy storage mechanism of $K_2V_3O_8$ cathode, electrochemical in situ XRD was conducted, as shown in Figures 3a and S5 [waterfall plot of the two dimensional (2D) mapping]. Figure 3a exhibits the in situ XRD patterns of $K_2V_3O_8$ during the initial cycles, ranging from 23–35.5 to 44.5–50°, respectively. The diffractive peaks and the corresponding crystal plane are marked at the bottom of the graph (a plastic wrap was used to seal the characterization window; the corresponding peak of the tape is located at 23.6°). In general, there are no obvious peaks shifting during the charge–discharge process, but the intensity of those peaks decreases dramatically and irreversibly, especially in the first charge process, indicating the amorphization of the cathode material. Owing to the amorphization of the structure, the cathode has more electrochemically active sites and faster ion diffusion kinetics.[46,47] This explains the decrease of the charge-transfer resistance in Figure 2b and the extraordinary rate performance in Figure 2c. Besides, the new peaks at 33.6 and 49.0° appear after the first charge process (activation process), indicating that a two-phase reaction occurs during the first discharge process, and the intensity of the new peaks are reversible and much stronger in the second and third cycle, reflecting a reversible two-phase reaction. Figure 3b shows the electrochemical in situ Raman characterization of the $K_2V_3O_8$ cathode (the waterfall plot of the 2D mapping is shown in Figure S6). Interestingly, the intensity of the band located at 891 cm^{-1}, 926, 464, and 526 cm^{-1} (which correspond to the $K_2V_3O_8$ cathode) change significantly as the charge-discharge cycling proceed: the intensities of the peaks first become weak and then reach the maximum at the end of the charge (discharge) stage. The change of band intensities is related to the distorted deformation of the [VO4] tetrahedron and the [VO5] pyramids,[48,49] which proves that both the extraction of K^+ (in the first charge process) and the insertion of Zn^{2+} (in the first discharge process) can influence the surrounding [VO4] tetrahedron and [VO5] pyramids and result in a structure distortion deformation.

Figure 4a–f shows the XPS results of V, Zn, and K elements (the XPS spectrum for all detected elements is shown in Figure S8). No obvious signals for Zn element (in Figure 4d) can be characterized in the XPS spectra of the original state and 1.6 V charged state of $K_2V_3O_8$; when discharged to 0.3 V, an evident Zn $2p_{3/2}$–$2p_{1/2}$ spin–orbit doublet is detected, demonstrating that the reversible two-phase reaction mentioned before is directly related to the storage of Zn ions. In addition, the original $K_2V_3O_8$ exhibits a V $2p_{3/2}$–$2p_{1/2}$ spin–orbit doublet for V(IV) and (V), in which the V $2p_{3/2}$ peak is located at 516.6 and 517.3 eV (Figure 4a), while the V $2p_{1/2}$ peak is located at 524.0 and 525.2 eV, respectively. In the 1.6 V charged state (Figure 4b), the intensity of the V^{4+} peak becomes weaker and that of the V^{5+} peak becomes stronger in comparison with that in the initial state, reflecting the oxidation of V^{4+} to V^{5+}; in the 0.3 V discharged state, the intensity of the V^{4+} peak strengthened and that of the V^{5+} peak weakened, reflecting the reduction of V^{4+} to V^{5+}. In Figure 4e,f, the change difference of V^{4+} and V^{5+} at a fully activated charged and discharged state is more obvious than that of the initially charged and discharged state, which means the extent of electrochemical reaction of the cathode is much deeper than the original state after full activation.

The irreversible K-ion extraction in the first cycle of the Zn//$K_2V_3O_8$ battery is mentioned previously, and we ascribe the excellent rate performance and cycle stability of the cathode to this process. Herein, it is of great importance to figure out the content change of K-ions in the cathode material during the first cycle. Thus, ex situ XPS and ICP were tested on the cathode under different charge–discharge states (the current density is 0.1 A g^{-1}). Figure 4g presents the ex situ XPS of K element. The intensity of K $2p_3$ and K $2p_1$ peaks continue to decline during the first cycle, indicating the irreversible extraction of the K-ions in the first charge–discharge process. Besides, the ex situ ICP characterization also supports the K-ion extraction theory. In the original state of $K_2V_3O_8$ cathode, the test value of the K/V substance amount ratio is 0.65, very close to the theoretical value (0.67), which proves the accuracy of the ICP characterization. With the proceeding of the

https://dx.doi.org/10.1021/acsami.9b21579
ACS Appl. Mater. Interfaces 2020, 12, 10420–10427

charge−discharge process, the K/V substance amount ratio declines from 0.65 to 0.29 as the battery charges to 1.6 V and then discharges to 0.3 V. Meanwhile, the K content decreases from 9.63 to 3.05%. Both ex situ XPS and ex situ ICP are proofs of the extraction of K-ions.

TGA conducted in Ar atmosphere with a temperature range of 35−700 °C in Figure S7 proved the formation of structural water during the first cycle. The weight loss of the initial electrode is 13.75 wt % (Figure S7a), while that of the 1.6 V charged state electrode and the 0.3 V discharged state electrode in the first cycle is 18.42 and 18.83 wt % (Figure S7b,c), respectively. According to Liang's work,[31] the extra weight loss is related to the structural water.

Based on the above ICP-MS, TGA, and in situ XRD results, we conclude that the K-ions irreversibly extract from the layered structure of the cathode, and structural water is formed in the charge−discharge process of first cycle, which can explain the 35 mA h g^{-1} capacity during the first charge process (Figure S2a) and cause the amorphization of crystal structure of cathode. In the first discharge process, a two-phase reaction occurred with the storage of Zn ions and extraction of K-ions. Combining the specific data of ICP-MS and TGA testing, the remaining content of K and the number of structural water molecular of the cathode can be calculated, so the specific electrode reaction of $Zn//K_2V_3O_8$ battery can be summarized as Figure 5 exhibits:

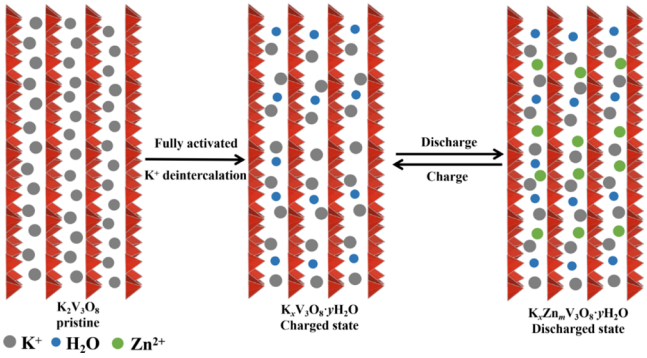

Figure 5. Schematic illustrations of energy storage mechanism of $K_2V_3O_8$ cathode during the first cycle.

In first charge process:
Cathode:

$$K_2V_3O_8 + 0.88H_2O = 1.04e^- + K_{0.96}V_3O_8\cdot 0.88H_2O + 1.04K^+ \quad (2)$$

Anode:

$$0.52Zn^{2+} + 1.04e^- = 0.52Zn \quad (3)$$

After full activation:
Cathode:

$$K_xV_3O_8\cdot yH_2O + mZn^{2+} + 2me^- = K_xZn_mV_3O_8\cdot yH_2O \quad (x < 0.96,\ y > 0.88) \quad (4)$$

Anode:

$$mZn = 2me^- + mZn^{2+} \quad (5)$$

The activation process is not finished at the end of the first charge process, it would last for several cycles, which explains the increase of specific capacity in Figure 2c,d. As Figures 4g,h and S7 show, the content of K-ions continues to decrease while the structural water content increases.

4. CONCLUSIONS

In summary, a high-performance rechargeable ZIB using a novel charging-optimized layered $K_2V_3O_8$ nanoflower as the cathode has been successfully assembled. We adopt the strategy of charging first to activate the cathode material, extracting K-ions from the interlayers of vanadium oxide through charging process, which creates more electrochemically active sites and decreases the charge-transfer resistance of the system. As a result, the electrochemical performance of the $Zn//K_2V_3O_8$ battery is impressive: a considerable specific capacity of 302.8 mA h g^{-1} at a current density of 0.1 A g^{-1}, as well as a remarkable cycling stability (92.3% capacity retention at 4 A g^{-1} for 2000 cycles) and extraordinary rate capability, is achieved. Besides, the energy storage mechanism was studied by in situ XRD, XPS, TGA, and ICP-MS. It is believed that this novel cathode material and the optimizing strategy will discover further possibilities to develop large-scale energy storage devices.

■ ASSOCIATED CONTENT

Supporting Information

The Supporting Information is available free of charge at https://pubs.acs.org/doi/10.1021/acsami.9b21579.

Experimental details, waterfall plot of in situ XRD and Raman, SEM, TG, electrochemical characterization, and other materials (PDF)

■ AUTHOR INFORMATION

Corresponding Author

Wen Luo − *State Key Laboratory of Advanced Technology for Materials Synthesis and Processing and Department of Physics, School of Science, Wuhan University of Technology, Wuhan 430070, China;* orcid.org/0000-0002-1732-295X; Email: luowen_1991@whut.edu.cn

Authors

Zhi Li − *State Key Laboratory of Advanced Technology for Materials Synthesis and Processing, Wuhan University of Technology, Wuhan 430070, China*

Buke Wu − *Department of Mechanical and Energy Engineering, Southern University of Science and Technology, Shenzhen 518055, China*

Mengyu Yan − *Department of Materials Science and Engineering, University of Washington, Seattle, Washington 98195, United States*

Liang He − *State Key Laboratory of Advanced Technology for Materials Synthesis and Processing, Wuhan University of Technology, Wuhan 430070, China; Department of Materials Science and NanoEngineering, Rice University, Houston, Texas 77005, United States;* orcid.org/0000-0002-7402-9194

Lin Xu − *State Key Laboratory of Advanced Technology for Materials Synthesis and Processing, Wuhan University of Technology, Wuhan 430070, China;* orcid.org/0000-0003-2347-288X

Guobin Zhang − *Department of Material Science and Engineering, City University of Hong Kong, Kowloon, Hong Kong 999077, China*

https://dx.doi.org/10.1021/acsami.9b21579
ACS Appl. Mater. Interfaces 2020, 12, 10420−10427

Tengfei Xiong − *Department of Chemistry, City University of Hong Kong, Kowloon, Hong Kong 999077, China*
Liqiang Mai − *State Key Laboratory of Advanced Technology for Materials Synthesis and Processing, Wuhan University of Technology, Wuhan 430070, China;* orcid.org/0000-0003-4259-7725

Complete contact information is available at: https://pubs.acs.org/10.1021/acsami.9b21579

Author Contributions

[▽]Z.L. and B.W. contributed equally.

Notes

The authors declare no competing financial interest.

■ ACKNOWLEDGMENTS

This work was supported by the National Natural Science Foundation of China (51904216), the National Natural Science Fund for Distinguished Young Scholars (51425204), the National Natural Science Foundation of China (51521001), the National Key Research and Development Program of China (2016YFA0202603), the Programme of Introducing Talents of Discipline to Universities (B17034), and the Yellow Crane Talent (Science & Technology) Program of Wuhan City.

■ REFERENCES

(1) Larcher, D.; Tarascon, J.-M. Towards Greener and More Sustainable Batteries for Electrical Energy Storage. *Nat. Chem.* **2015**, *7*, 19−29.
(2) Yang, Z.; Zhang, J.; Kintner-Meyer, M. C. W.; Lu, X.; Choi, D.; Lemmon, J. P.; Liu, J. Electrochemical Energy Storage for Green Grid. *Chem. Rev.* **2011**, *111*, 3577−3613.
(3) Mai, L.; Tian, X.; Xu, X.; Chang, L.; Xu, L. Nanowire Electrodes for Electrochemical Energy Storage Devices. *Chem. Rev.* **2014**, *114*, 11828−11862.
(4) Winter, M.; Brodd, R. J. What Are Batteries, Fuel Cells, and Supercapacitors? *Chem. Rev.* **2004**, *105*, 4245.
(5) Liu, Y.; Shen, Q.; Zhao, X.; Zhang, J.; Liu, X.; Wang, T.; Zhang, N.; Jiao, L.; Chen, J.; Fan, L. Z. Hierarchical Engineering of Porous P2-$Na_{2/3}Ni_{1/3}Mn_{2/3}O_2$ Nanofibers Assembled by Nanoparticles Enables Superior Sodium-Ion Storage Cathodes. *Adv. Funct. Mater.* **2020**, *30*, 1907837.
(6) Wang, F.; Zhang, N.; Zhao, X.; Wang, L.; Zhang, J.; Wang, T.; Liu, F.; Liu, Y.; Fan, L. Z. Realizing a High-Performance Na-Storage Cathode by Tailoring Ultrasmall Na_2FePO_4F Nanoparticles with Facilitated Reaction Kinetics. *Adv. Sci.* **2019**, *6*, 1900649.
(7) Sun, Y.-K.; Chen, Z.; Noh, H.-J.; Lee, D.-J.; Jung, H.-G.; Ren, Y.; Wang, S.; Yoon, C. S.; Myung, S.-T.; Amine, K. Nanostructured High-Energy Cathode Materials for Advanced Lithium Batteries. *Nat. Mater.* **2012**, *11*, 942−947.
(8) Goodenough, J. B.; Kim, Y. Challenges for Rechargeable Li Batteries. *Chem. Mater.* **2010**, *22*, 587−603.
(9) Zhang, G.; Xiong, T.; Pan, X.; Zhao, Y.; Yan, M.; Zhang, H.; Wu, B.; Zhao, K.; Mai, L. Illumining phase transformation dynamics of vanadium oxide cathode by multimodal techniques under operando conditions. *Nano Res.* **2019**, *12*, 905−910.
(10) Whittingham, M. S. Lithium Batteries and Cathode Materials. *Chem. Rev.* **2004**, *104*, 4271−4302.
(11) Idota, Y.; Kubota, T.; Matsufuji, A.; Maekawa, Y.; Miyasaka, T. Tin-Based Amorphous Oxide: A High-Capacity Lithium-Ion-Storage Material. *Science* **1997**, *276*, 1395−1397.
(12) Bruce, P. G.; Freunberger, S. A.; Hardwick, L. J.; Tarascon, J.-M. Li−O_2 and Li−S Batteries with High Energy Storage. *Nat. Mater.* **2012**, *11*, 19−29.
(13) Xu, C.; Li, B.; Du, H.; Kang, F. Energetic Zinc Ion Chemistry: The Rechargeable Zinc Ion Battery. *Angew. Chem., Int. Ed.* **2012**, *51*, 933−935.
(14) Lee, B.-S.; Cui, S.; Xing, X.; Liu, H.; Yue, X.; Petrova, V.; Lim, H.-D.; Chen, R.; Liu, P. Dendrite Suppression Membranes for Rechargeable Zinc Batteries. *ACS Appl. Mater. Interfaces* **2018**, *10*, 38928−38935.
(15) Wang, X.; Ma, L.; Zhang, P.; Wang, H.; Li, S.; Ji, S.; Wen, Z.; Sun, J. Vanadium Pentoxide Nanosheet as Cathode for Aqueous Zinc-ion Batteries with High Rate and Long Durability. *Appl. Surf. Sci.* **2020**, *502*, 144207.
(16) Zhang, N.; Cheng, F.; Liu, J.; Wang, L.; Long, X.; Liu, X.; Li, F.; Chen, J. Rechargeable Aqueous Zinc-Manganese Dioxide Batteries with High Energy and Power Densities. *Nat. Commun.* **2017**, *8*, 405.
(17) Kundu, D.; Adams, B.; Duffort, V.; Vajargah, S.; Nazar, L. A High-Capacity and Long-Life Aqueous Rechargeable Zinc Battery Using A Metal Oxide Intercalation Cathode. *Nat. Energy* **2016**, *1*, 16119.
(18) Pan, H.; Shao, Y.; Yan, P.; Cheng, Y.; Han, K.; Nie, Z.; Wang, C.; Yang, J.; Li, X.; Bhattacharya, P.; Mueller, K.; Liu, J. Reversible Aqueous Zinc/Manganese Oxide Energy Storage from Conversion Reactions. *Nat. Energy* **2016**, *1*, 16039.
(19) Yan, M.; He, P.; Chen, Y.; Wang, S.; Wei, Q.; Zhao, K.; Xu, X.; An, Q.; Shuang, Y.; Shao, Y.; Mueller, K. T.; Mai, L.; Liu, J.; Yang, J. Water-Lubricated Intercalation in $V_2O_5{\cdot}nH_2O$ for High-Capacity and High-Rate Aqueous Rechargeable Zinc Batteries. *Adv. Mater.* **2018**, *30*, 1703725.
(20) He, P.; Zhang, G.; Liao, X.; Yan, M.; Xu, X.; An, Q.; Liu, J.; Mai, L. Sodium Ion Stabilized Vanadium Oxide Nanowire Cathode for High-Performance Zinc-Ion Batteries. *Adv. Energy Mater.* **2018**, *8*, 1702463.
(21) He, P.; Yan, M.; Zhang, G.; Sun, R.; Chen, L.; An, Q.; Mai, L. Layered VS_2 Nanosheet-Based Aqueous Zn Ion Battery Cathode. *Adv. Energy Mater.* **2017**, *7*, 1601920.
(22) Zhang, N.; Jia, M.; Dong, Y.; Wang, Y.; Xu, J.; Liu, Y.; Jiao, L.; Cheng, F. Hydrated Layered Vanadium Oxide as a Highly Reversible Cathode for Rechargeable Aqueous Zinc Batteries. *Adv. Funct. Mater.* **2019**, *29*, 1807331.
(23) Zhang, N.; Dong, Y.; Jia, M.; Bian, X.; Wang, Y.; Qiu, M.; Xu, J.; Liu, Y.; Jiao, L.; Cheng, F. Rechargeable Aqueous Zn−V_2O_5 Battery with High Energy Density and Long Cycle Life. *ACS Energy Lett.* **2018**, *3*, 1366−1372.
(24) Liu, Z.; Pulletikurthi, G.; Endres, F. A Prussian Blue/Zinc Secondary Battery with a Bio-Ionic Liquid−Water Mixture as Electrolyte. *ACS Appl. Mater. Interfaces* **2016**, *8*, 12158−12164.
(25) Trócoli, R.; La Mantia, F. An Aqueous Zinc-Ion Battery Based on Copper Hexacyanoferrate. *ChemSusChem* **2015**, *8*, 481−485.
(26) Gupta, T.; Kim, A.; Phadke, S.; Biswas, S.; Luong, T.; Hertzberg, B. J.; Chamoun, M.; Evans-Lutterodt, K.; Steingart, D. A. Improving the Cycle Life of A High-Rate, High-Potential Aqueous Dual-Ion Battery Using Hyper-Dendritic Zinc and Copper Hexacyanoferrate. *J. Power Sources* **2016**, *305*, 22−29.
(27) Hou, Z.; Zhang, X.; Li, X.; Zhu, Y.; Liang, J.; Qian, Y. Surfactant Widens the Electrochemical Window of An Aqueous Electrolyte for Better Rechargeable Aqueous Sodium/zinc battery. *J. Mater. Chem. A* **2017**, *5*, 730−738.
(28) Zhang, L.; Chen, L.; Zhou, X.; Liu, Z. Morphology-Dependent Electrochemical Performance of Zinc Hexacyanoferrate Cathode for Zinc-Ion Battery. *Sci. Rep.* **2015**, *5*, 18263.
(29) Sun, K. E. K.; Hoang, T. K. A.; Doan, T. N. L.; Yu, Y.; Zhu, X.; Tian, Y.; Chen, P. Suppression of Dendrite Formation and Corrosion on Zinc Anode of Secondary Aqueous Batteries. *ACS Appl. Mater. Interfaces* **2017**, *9*, 9681−9687.
(30) Wang, F.; Sun, W.; Shadike, Z.; Hu, E.; Ji, X.; Gao, T.; Yang, X.-Q.; Xu, K.; Wang, C. How Water Accelerates Bivalent Ion Diffusion at the Electrolyte/Electrode Interface. *Angew. Chem., Int. Ed.* **2018**, *57*, 11978−11981.
(31) Yang, Y.; Tang, Y.; Fang, G.; Shan, L.; Guo, J.; Zhang, W.; Wang, C.; Wang, L.; Zhou, J.; Liang, S. Li^+ Intercalated $V_2O_5{\cdot}nH_2O$

with Enlarged Layer Spacing and Fast Ion Diffusion as An Aqueous Zinc-Ion Battery Cathode. *Energy Environ. Sci.* **2018**, *11*, 3157−3162.
(32) Tang, B.; Zhou, J.; Fang, G.; Liu, F.; Zhu, C.; Wang, C.; Pan, A.; Liang, S. Engineering the Interplanar Spacing of Ammonium Vanadates as A High-Performance Aqueous Zinc-Ion Battery Cathode. *J. Mater. Chem. A* **2019**, *7*, 940−945.
(33) Tang, B.; Fang, G.; Zhou, J.; Wang, L.; Lei, Y.; Wang, C.; Lin, T.; Tang, Y.; Liang, S. Potassium Vanadates with Stable Structure and Fast Ion Diffusion Channel as Cathode for Rechargeable Aqueous Zinc-Ion Batteries. *Nano Energy* **2018**, *51*, 579−587.
(34) Zhao, Y.; Han, C.; Yang, J.; Su, J.; Xu, X.; Li, S.; Xu, L.; Fang, R.; Jiang, H.; Zou, X.; Song, B.; Mai, L.; Zhang, Q. Stable Alkali Metal Ion Intercalation Compounds as Optimized Metal Oxide Nanowire Cathodes for Lithium Batteries. *Nano Lett.* **2015**, *15*, 2180−2185.
(35) Huang, J.; Wang, Z.; Hou, M.; Dong, X.; Liu, Y.; Wang, Y.; Xia, Y. Polyaniline-Intercalated Manganese Dioxide Nanolayers as A High-Performance Cathode Material for An Aqueous Zinc-Ion Battery. *Nat. Commun.* **2018**, *9*, 2906.
(36) Cheng, F. Y.; Chen, J.; Gou, X. L.; Shen, P. W. High-Power Alkaline Zn−MnO_2 Batteries Using γ-MnO_2 Nanowires/Nanotubes and Electrolytic Zinc Powder. *Adv. Mater.* **2005**, *17*, 2753−2756.
(37) Wu, B.; Zhang, G.; Yan, M.; Xiong, T.; He, P.; He, L.; Xu, X.; Mai, L. Graphene Scroll-Coated α-MnO_2 Nanowires as High-Performance Cathode Materials for Aqueous Zn-Ion Battery. *Small* **2018**, *14*, 1703850.
(38) Tu, F.; Wu, T.; Liu, S.; Jin, G.; Pan, C. Facile Fabrication of MnO_2 Nanorod/Graphene Hybrid as Cathode Materials for Lithium Batteries. *Electrochim. Acta* **2013**, *106*, 406−410.
(39) Hardcastle, F. D.; Wachs, I. E. Determination of Vanadium-Oxygen Bond Distances and Bond Orders by Raman Spectroscopy. *J. Phys. Chem.* **1991**, *95*, 5031−5041.
(40) Stancovski, V.; Badilescu, S. In situ Raman Spectroscopic−Electrochemical Studies of Lithium-Ion Battery Materials: A Historical Overview. *J. Appl. Electrochem.* **2014**, *44*, 23−43.
(41) Jian, Z.; Zheng, M.; Liang, Y.; Zhang, X.; Gheytani, S.; Lan, Y.; Shi, Y.; Yao, Y. Li_3VO_4 Anchored Graphene Nanosheets for Long-Life and High-Rate Lithium-Ion Batteries. *Chem. Commun.* **2015**, *51*, 229−231.
(42) Shi, Y.; Wang, J.-Z.; Chou, S.-L.; Wexler, D.; Li, H.-J.; Ozawa, K.; Liu, H.-K.; Wu, Y.-P. Hollow Structured Li_3VO_4 Wrapped with Graphene Nanosheets in Situ Prepared by a One-Pot Template-Free Method as an Anode for Lithium-Ion Batteries. *Nano Lett.* **2013**, *13*, 4715−4720.
(43) Augustyn, V.; Come, J.; Lowe, M. A.; Kim, J. W.; Taberna, P.-L.; Tolbert, S. H.; Abruña, H. D.; Simon, P.; Dunn, B. High-Rate Electrochemical Energy Storage through Li^+ Intercalation Pseudocapacitance. *Nat. Mater.* **2013**, *12*, 518−522.
(44) Wang, H.; Zhu, C.; Chao, D.; Yan, Q.; Fan, H. J. Nonaqueous Hybrid Lithium-Ion and Sodium-Ion Capacitors. *Adv. Mater.* **2017**, *29*, 1702093.
(45) Augustyn, V.; Simon, P.; Dunn, B. Pseudocapacitive Oxide Materials for High-Rate Electrochemical Energy Storage. *Energy Environ. Sci.* **2014**, *7*, 1597−1614.
(46) Chae, O. B.; Kim, J.; Park, I.; Jeong, H.; Ku, J. H.; Ryu, J. H.; Kang, K.; Oh, S. M. Reversible Lithium Storage at Highly Populated Vacant Sites in an Amorphous Vanadium Pentoxide Electrode. *Chem. Mater.* **2014**, *26*, 5874−5881.
(47) Sheng, J.; Li, Q.; Wei, Q.; Zhang, P.; Wang, Q.; Lv, F.; An, Q.; Chen, W.; Mai, L. Metastable Amorphous Chromium-Vanadium Oxide Nanoparticles with Superior Performance as A New Lithium Battery Cathode. *Nano Res.* **2014**, *7*, 1604−1612.
(48) Choi, K.-Y.; Lemmens, P.; Gnezdilov, V. P.; Sales, B. C.; Lumsden, M. D. Coupling of Spin and Lattice Modes in the S=1/2 Two-Dimensional Antiferromagnet $K_2V_3O_8$ with Magneto-Dielectric Couplings. *Phys. Rev. B: Condens. Matter Mater. Phys.* **2012**, *85*, 144434.
(49) Bao, Q.; Bao, S.; Li, C. M.; Qi, X.; Pan, C.; Zang, J.; Wang, W.; Tang, D. Y. Lithium Insertion in Channel-Structured β-$AgVO_3$: In-Situ Raman Study and Computer Simulation. *Chem. Mater.* **2007**, *19*, 5965−5972.

https://dx.doi.org/10.1021/acsami.9b21579
ACS Appl. Mater. Interfaces 2020, 12, 10420−10427